Crystal-field effects in the kagome antiferromagnet $Ho_3Ru_4Al_{12}$

D. I. Gorbunov,[1] T. Nomura,[1] I. Ishii,[2] M. S. Henriques,[3] A. V. Andreev,[3] M. Doerr,[4] T. Stöter,[4] T. Suzuki,[2] S. Zherlitsyn,[1] and J. Wosnitza[1,4]

[1]*Hochfeld-Magnetlabor Dresden (HLD-EMFL), Helmholtz-Zentrum Dresden-Rossendorf, 01328 Dresden, Germany*
[2]*Department of Quantum Matter, ADSM, Hiroshima University, Higashi-Hiroshima 739-8530, Japan*
[3]*Institute of Physics, Academy of Sciences, Na Slovance 2, 182 21 Prague, Czech Republic*
[4]*Institut für Festkörper- und Materialphysik, TU Dresden, 01062 Dresden, Germany*

(Received 9 February 2018; revised manuscript received 28 March 2018; published 8 May 2018)

In $Ho_3Ru_4Al_{12}$, the Ho atoms form a distorted kagome lattice. We performed magnetization, magnetic-susceptibility, specific-heat, and ultrasound measurements on a single crystal. We find that the magnetic and magnetoelastic properties of $Ho_3Ru_4Al_{12}$ result from an interplay between geometric frustration and crystal-electric-field (CEF) effects. The Ho atoms order antiferromagnetically at $T_N = 4.5$ K with reduced magnetic moments. In applied field, the magnetization shows anomalies that can be explained by CEF level crossings. We propose a CEF level scheme for which the ground-state doublet and the first two excited singlets at about 2.7 K form a quasiquartet. Indirect interlevel transitions allow for a quadrupolar interaction. This interaction explains well changes in the elastic shear modulus C_{44} as a function of temperature and magnetic field.

DOI: 10.1103/PhysRevB.97.184412

I. INTRODUCTION

Geometric frustration arises when the spatial spin arrangement leads to competing interactions that cannot be satisfied simultaneously (for a review, see, e.g., Refs. [1,2]). Such frustration, therefore, prevents or largely hampers the development of long-range magnetic order and frequently leads to the emergence of novel, often exotic states. For example, for materials with a pyrochlore lattice where spins reside in corner-sharing tetrahedra, spin-glass, spin-liquid, and spin-ice states have been observed experimentally or predicted theoretically [3–9].

Intermetallic compounds with the general formula $R_3Ru_4Al_{12}$ (R = rare-earth atom or U) crystallize in the hexagonal crystal structure of $Gd_3Ru_4Al_{12}$ type (space group $P6_3/mmc$ with two formula units per elementary cell) [10–12]. Two types of layers perpendicular to the [001] axis can be distinguished [Fig. 1(a)]. The layers containing the R and Al atoms have the composition R_3Al_4 and are planar, whereas those containing the Ru and Al atoms as Ru_4Al_8 are slightly corrugated. The R atoms occupy one crystallographic site and form triangular nets parallel to the basal plane. The projection of the unit cell onto the (001) plane shows that the R atoms are arranged in distorted kagome nets [Fig. 1(b)]. The distortion manifests through two types of equilateral triangles [thick magenta lines in Fig. 1(b)]. The distances between the Ho atoms are about 3.7 and 5.1 Å for the smaller and larger triangles, respectively. Since the R atoms form the kagome lattice, their magnetic moments are prone to geometric frustration. Although partially released, the geometric frustration has been found to lead to complex magnetic structures and rich phase diagrams for a number of $R_3Ru_4Al_{12}$ compounds [13–26].

$R_3Ru_4Al_{12}$ with R = Pr and Nd are ferromagnets [13–16], whereas those with R = Gd, Tb, Dy, and U are antiferromagnets [17–26]. Just below the Curie temperature, $Pr_3Ru_4Al_{12}$ and $Nd_3Ru_4Al_{12}$ display collinear ferromagnetic structures for which the only crystallographic site of the R element splits into two magnetic positions that carry different magnetic moments [15,16]. For $Pr_3Ru_4Al_{12}$, a spin-reorientation phase transition occurs to a noncollinear magnetic structure with decreasing temperature [16].

The antiferromagnetic counterparts also show noncollinear magnetic structures. For $Dy_3Ru_4Al_{12}$, the moments are aligned predominantly along the [001] axis [20], whereas for $U_3Ru_4Al_{12}$ the moments form a triangular pattern within the basal plane [26]. In applied magnetic fields, the compounds with R = Tb, Dy, and Yb display field-induced phase transitions [18–21,23,24]. Most of the transitions are accompanied by large magnetoresistance changes due to the strong interaction between the conduction electrons and the localized moments.

Although $R_3Ru_4Al_{12}$ compounds have been investigated for several years, the role of crystal-electric-field (CEF) effects in the physics of these materials has not been studied. The CEF is the main source of the magnetocrystalline anisotropy in intermetallic compounds based on rare-earth elements [27]. While the crystal-field parameters can in general be extracted from magnetization measurements of ferro- and ferrimagnets [28,29], antiferromagnets are more challenging systems that require a different approach.

Here, we study a new member of the $R_3Ru_4Al_{12}$ family, $Ho_3Ru_4Al_{12}$, by magnetization, magnetic-susceptibility, specific-heat, and ultrasound measurements. We find that $Ho_3Ru_4Al_{12}$ orders antiferromagnetically at $T_N = 4.5$ K. In applied fields, pronounced anomalies are observed in the magnetization and elastic moduli, signaling a strong magnetoelastic coupling. Moreover, we find a softening in a transverse elastic modulus upon approaching T_N. Our CEF analysis shows that the ground-state doublet and the first two excited singlets at about 2.7 K form a quasiquartet in $Ho_3Ru_4Al_{12}$. This suggests

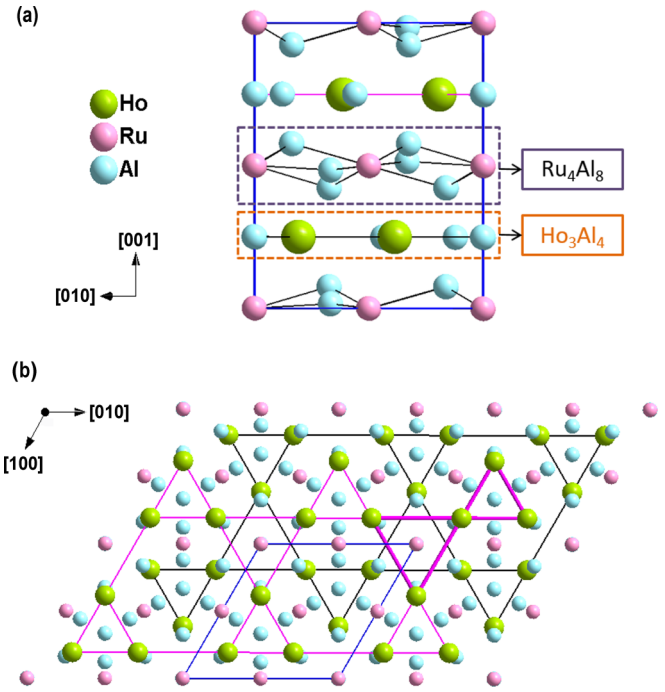

FIG. 1. Crystal structure of $Ho_3Ru_4Al_{12}$: (a) the unit cell and (b) the projection onto the basal plane showing the unit cell (dark blue) and the Ho atoms (Wyckoff site 6*h*) forming corner-sharing triangles of a distorted kagome lattice (black for the lower layer and magenta for the upper layer). In the upper layer, two types of triangles are shown by thick magenta lines.

an interlevel quadrupole interaction between the ground state and the first excited states, leading to the elastic softening. Further, we observe reduced Ho magnetic moments whose magnitude cannot be explained by the CEF alone. We therefore conclude that the Ho moments are ordered incompletely below T_N, probably due to geometric frustration.

II. EXPERIMENTAL DETAILS

A $Ho_3Ru_4Al_{12}$ single crystal was grown from a quasistoichiometric mixture of the pure elements (99.9% Ho, 99.99% Ru, and 99.999% Al) with an Al mass excess of 1% in a tri-arc furnace by a modified Czochralski method on a rotating water-cooled Cu crucible in protective Ar atmosphere. In order to orient the crystal and cut the samples for magnetization, magnetic-susceptibility, specific-heat, and ultrasound measurements, backscattered Laue patterns were used (Fig. 1S in the Supplemental Material [30]).

The structural details of $Ho_3Ru_4Al_{12}$ were checked by performing single-crystal x-ray diffraction on a small crystal of dimensions $0.23 \times 0.17 \times 0.10$ mm^3 glued on the top of a glass fiber and mounted onto a goniometer head. The diffracted intensities were collected at room temperature using the four-circle diffractometer Gemini of Agilent, equipped with a Mo x-ray tube [λ(MoKα = 0.71073 Å)], Mo-enhanced collimator, graphite monochromator, and an Atlas CCD detector. The CRYSALIS [31] software was employed to collect, inspect, integrate, and reduce the data. The absorption correction was performed using face indexing of the crystal shape in combination with a Gaussian correction based on spherical harmonic functions. The program SUPERFLIP [32] was used for the structure solution and the JANA2006 package [33] for the structure refinement. The refinement confirmed the correctness of our structural model, with the *R* factor converging to $R_{obs} = 2.9\%$. The lattice parameters are $a = 8.7522(6)$ Å and $c = 9.5075(6)$ Å. Refined atomic positions and equivalent isotropic displacement parameters are given in Table I.

TABLE I. Refined atomic coordinates, x, y, z, equivalent isotropic displacement parameters, U_{eq}, and their estimated standard deviations for $Ho_3Ru_4Al_{12}$.

Atom	Wyckoff position	x	y	z	U_{eq}
Ho	6*h*	0.19281(4)	0.38563(8)	1/4	0.0056(2)
Ru1	2*a*	0	0	0	0.0043(4)
Ru2	6*g*	0.5	0.5	0	0.0040(3)
Al1	6*h*	0.5606(2)	0.4394(2)	1/4	0.0042(7)
Al2	12*k*	0.3249(4)	0.16245(2)	0.0770(3)	0.0056(6)
Al3	4*f*	1/3	2/3	0.0156(5)	0.0051(9)
Al4	2*b*	0	0	1/4	0.0079(9)

The field and temperature dependences of the magnetization and magnetic susceptibility (excitation amplitude 0.001 T, frequency 97 Hz) up to 14 T were measured between 2 and 300 K for fields applied along the principal crystallographic directions, [100], [120], and [001], of a 60-mg sample using a Physical Property Measurement System. The specific heat was measured by use of the relaxation method in magnetic fields between 0 and 14 T applied along the [001] axis.

The field and temperature dependences of the relative sound-velocity changes, $\Delta v/v$, were measured using an ultrasound pulse-echo technique [34,35] in static fields up to 2 T and in pulsed fields up to 58 T. We approximated the relative changes of the elastic moduli, $\Delta C_{ii}/C_{ii}$, using $\Delta C_{ii}/C_{ii} = 2\Delta v_{ii}/v_{ii}$. A pair of piezoelectric transducers were glued to opposite surfaces of the sample in order to excite and detect acoustic waves. We measured the longitudinal, C_{11} ($\boldsymbol{k} \parallel \boldsymbol{u} \parallel [100]$, where $\boldsymbol{k}$ and $\boldsymbol{u}$ are the wave vector and polarization of acoustic waves, respectively), C_{33} ($\boldsymbol{k} \parallel \boldsymbol{u} \parallel [001]$), and transverse, C_{44} ($\boldsymbol{k} \parallel [100], \boldsymbol{u} \parallel [001]$), C_{66} ($\boldsymbol{k} \parallel [100], \boldsymbol{u} \parallel [120]$) elastic moduli.

High-field magnetization was measured at 1.5 K in pulsed magnetic fields up to 58 T (pulse duration 25 ms) by the induction method using a coaxial pickup coil system. The absolute values of the magnetization were calibrated using static-field data. A detailed description of the high-field magnetometer is given in Ref. [36].

III. RESULTS

The temperature dependences of the magnetic susceptibility, χ, of $Ho_3Ru_4Al_{12}$ are shown in Fig. 2(a). There is a large anisotropy between the basal plane and the [001] axis. For field applied along the [001] axis, the susceptibility starts to increase more rapidly near 3 K with decreasing temperature.

The specific heat, C, displays a rather broad anomaly near 4 K [Fig. 2(b)] indicating the ordering of the Ho moments at $T_N = 4.5$ K. This T_N value is confirmed by our

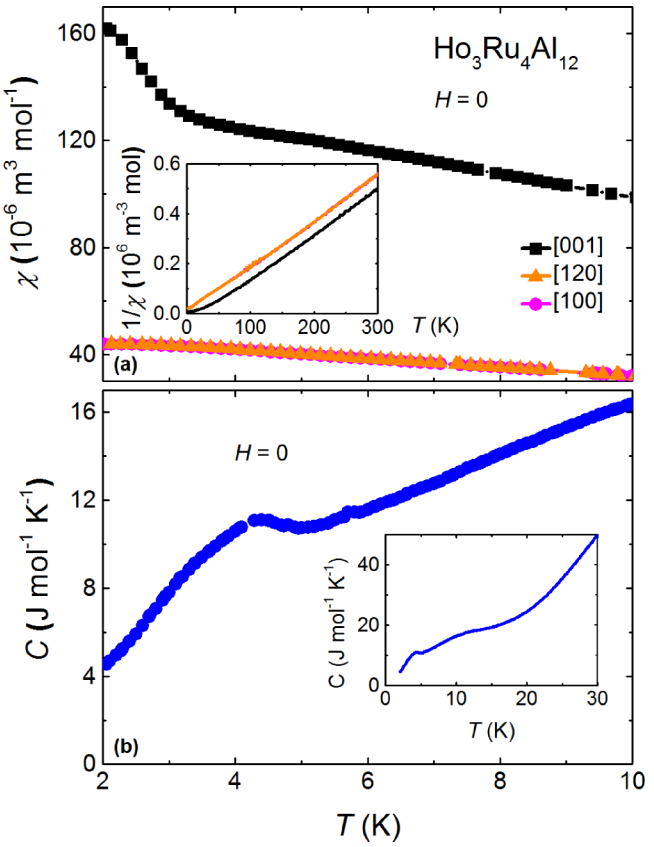

FIG. 2. Temperature dependences of (a) the magnetic susceptibility, χ, and (b) the specific heat, C, of $Ho_3Ru_4Al_{12}$. The insets in panels (a) and (b) show the inverse magnetic susceptibility, $1/\chi$, between 2 and 300 K, and C between 2 and 30 K, respectively.

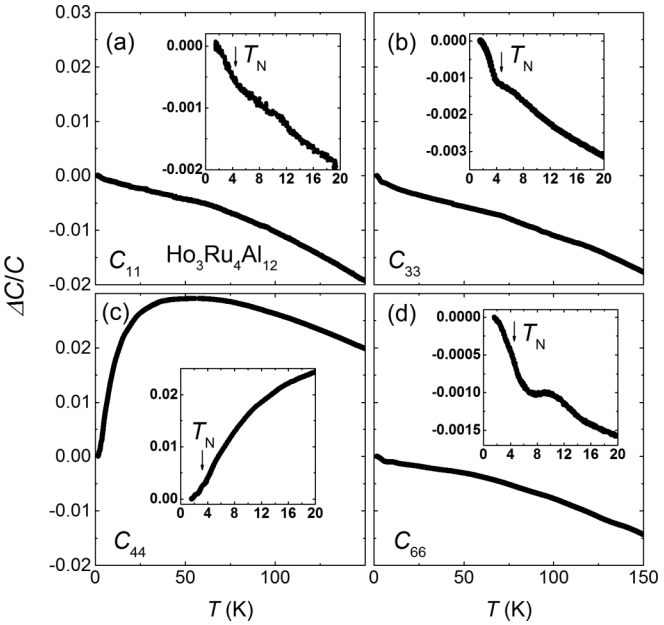

FIG. 3. Temperature dependences of the relative change of the elastic moduli (a) C_{11}, (b) C_{33}, (c) C_{44}, and (d) C_{66} of $Ho_3Ru_4Al_{12}$ at zero field. The insets show the vicinity of T_N. The ultrasound frequencies were 53, 51, 185, and 114 MHz for the C_{11}, C_{33}, C_{44}, and C_{66} modes, respectively,

neutron-diffraction study [37]. At around 12 K, an additional, Schottky-like anomaly is observed in the specific heat [inset in Fig. 2(b)].

Above 100 K, the temperature-dependent inverse magnetic susceptibility, $1/\chi$, follows Curie-Weiss laws [inset in Fig. 2(a)]:

$$\chi = \frac{C_0}{T-\theta}, \tag{1}$$

where C_0 is the Curie constant proportional to the square of the effective magnetic moment μ_{eff}, and θ is the Weiss or paramagnetic Curie temperature. The obtained μ_{eff} and θ values are listed in Table II. The effective magnetic moment per Ho atom is found to be 10.7(1) μ_B for the [100] and [120] and 10.8(1) μ_B for the [001] field directions. This is close to the theoretical value, 10.6 μ_B, for a Ho^{3+} ion. The positive θ values reflect the dominance of ferromagnetic exchange interactions.

TABLE II. Effective magnetic moments, μ_{eff}, per Ho atom and paramagnetic Curie temperatures, θ, for fields applied along the principal crystallographic directions of $Ho_3Ru_4Al_{12}$ obtained from fits in the listed temperature ranges.

	H || [100]	H || [120]	H || [001]
μ_{eff} (μ_B/Ho)	10.7(1)	10.7(1)	10.8(1)
θ (K)	1(1)	1(1)	27(1)
Temperature range (K)	100–300	100–300	100–300

Figure 3 shows the temperature dependences of all measured elastic moduli. The longitudinal C_{11} and C_{33} and the transverse C_{66} moduli increase monotonically with decreasing temperature [Figs. 3(a), 3(b) and 3(d)]. By contrast, the transverse modulus C_{44} exhibits a pronounced softening of 3% below 50 K [Fig. 3(c)]. The softening is due to CEF effects discussed below. In the vicinity of T_N, C_{11} and C_{44} show a change of slope [insets in Figs. 3(a) and 3(c)]. C_{33} exhibits a clear kink and upturn at the phase transition into the ordered state [inset in Fig. 3(b)]. C_{66} shows additional hardening at low temperatures preceded by a local maximum at 10 K [inset in Fig. 3(d)].

Important information on the magnetic order of $Ho_3Ru_4Al_{12}$ can be obtained from the magnetization, M [Fig. 4(a)]. There is no spontaneous magnetic moment for any chosen direction, as can be expected for an antiferromagnetic state. A large anisotropy is observed for fields applied along the [001] axis and in the basal plane. The [001] axis is the easy magnetization direction. This suggests that in the ground state, the largest projection of the Ho magnetic moments in zero field is along the [001] direction. The magnetic order originates mainly from the spin degrees of freedom of the ground-state doublet, as can be concluded from the CEF level scheme (see Sec. IV). For a field applied along the easy axis, two anomalies can be resolved at 0.3 and 0.8 T. In addition to these features, the field derivative of the magnetization, dM/dH, shows also a broad maximum at 1.4 T.

The change in the magnetic state leads to pronounced anomalies in the elastic moduli [Fig. 4(b)]. With increasing field, C_{11}, C_{33}, and C_{66} display a softening, while C_{44}

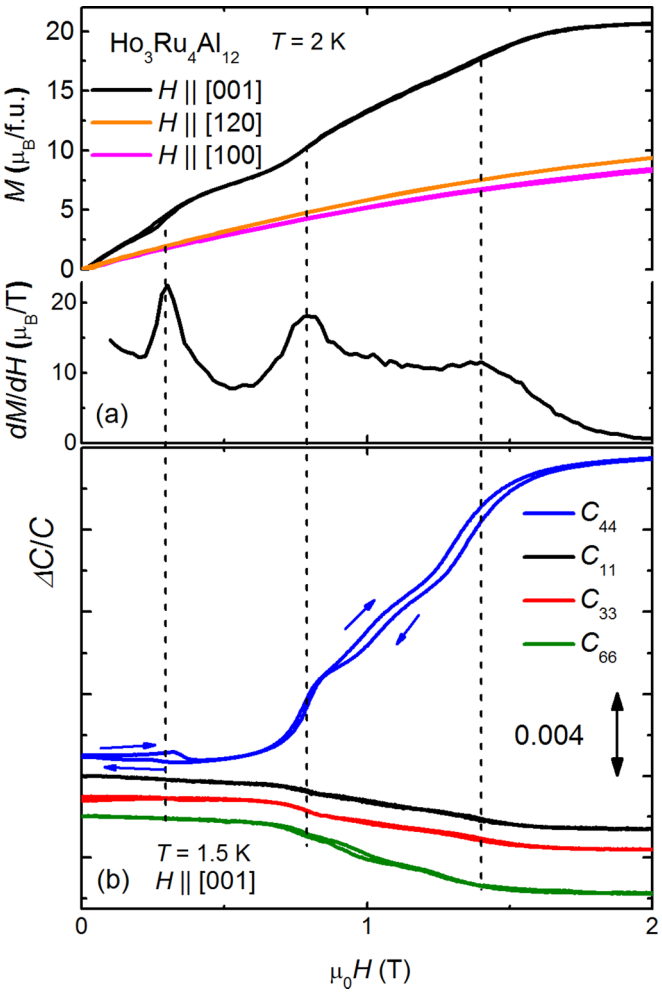

FIG. 4. Field dependences of (a) the magnetization, M, and the field derivative of the magnetization, dM/dH, at 2 K and (b) the relative changes of the elastic moduli C_{11}, C_{33}, C_{44}, and C_{66} of $Ho_3Ru_4Al_{12}$ at 1.5 K. The ultrasound frequencies were 71, 57, 185, and 114 MHz for the C_{11}, C_{33}, C_{44}, and C_{66} modes, respectively.

increases and shows much larger changes. The steep increase of $\Delta C_{44}/C_{44}$ at 0.8 and 1.4 T is of the order of 0.5%. At elevated temperatures, anomalies in the elastic moduli broaden (Fig. 2S in the Supplemental Material [30]).

Although our static-field magnetization data up to 2 T show similar values for fields applied along the [100] and [120] directions, measurements in pulsed fields up to 58 T reveal a large anisotropy within the basal plane at higher fields (Fig. 5). The [100]-axis magnetization displays a weak S shape [Fig. 5(a)]. It is centered around 31 T, as can be seen more clearly from the dM/dH vs H data. For fields aligned along the [120] axis, a more pronounced S shape develops near 25 T [Fig. 5(b)]. These features signal a transformation of the magnetic structure induced by magnetic fields. For fields applied along the [001] direction, no anomalies are observed above 2 T [Fig. 5(c)]. Using the localized magnetic moment of a Ho^{3+} ion, $M_{Ho} = 10\,\mu_B$, the magnetization of the fully polarized state can be estimated as $M_{ferro} = 3 \times M_{Ho} = 30\,\mu_B$/f.u. This state is not reached at 58 T applied along any of the crystallographic directions. The high-field behavior of $Ho_3Ru_4Al_{12}$ is a result of the competition between the CEF effect and geometric frustration, as will be discussed below.

To explore this phenomenon further, we have measured C_{44} in pulsed magnetic fields [Figs. 5(d), 5(e) and 5(f)]. Here, C_{44} signals the presence of broad metastable regions. For fields applied along [100] at 1.4 K, C_{44} first grows by approximately 3% [Fig. 5(d)]. Then this modulus displays a minimum at 18 T. With decreasing field, two minima are observed at 16 and 7 T. There is a hysteresis in the field range where the magnetization shows an S shape.

At 4.2 K, C_{44} shows similar features with a hysteretic region up to almost 40 T. Two anomalies and a large hysteresis are still present even above T_N, at 6.7 K. At higher temperatures, these features disappear.

For fields applied along the [120] axis at 1.3 K, C_{44} displays hardening slightly above the field-induced transition found in the magnetization [Fig. 5(e)]. A broad hysteresis is evident in C_{44} from low fields to beyond 40 T. With increasing temperature, the hysteresis weakens and is no longer observed above T_N. Reasons for the metastable state are unclear.

Interestingly, for fields applied along [001] we observe a small hysteretic feature in C_{44} whose position changes linearly with temperature [Fig. 5(f)]. The origin of this anomaly is the subject of further investigations.

IV. CEF ANALYSIS

The physical properties of $Ho_3Ru_4Al_{12}$ are likely affected by the CEF and geometric frustration. In order to examine their role, we performed a thorough CEF analysis. We consider the effective Hamiltonian,

$$H_{eff} = H_{CEF} + H_{sQ} + H_{QQ} + H_{Zeeman}, \tag{2}$$

where H_{CEF}, H_{sQ}, H_{QQ}, and H_{Zeeman} are the CEF, strain-quadrupole, quadrupole-quadrupole, and Zeeman energy, respectively. The CEF term in the hexagonal symmetry is given by

$$H_{CEF} = B_2{}^0 O_2{}^0 + B_4{}^0 O_4{}^0 + B_6{}^0 O_6{}^0 + B_6{}^6 O_6{}^6, \tag{3}$$

where B_m^n are crystal-field parameters and O_m^n are Stevens' equivalent operators tabulated in Ref. [38]. The strain-quadrupole interaction is given by

$$H_{sQ} = -\sum_i g_i O_i \varepsilon_i, \tag{4}$$

where g_i is the strain-quadrupole coupling constant, O_i the quadrupole operator, and ε_i the strain. The quadrupole-quadrupole interaction can be expressed as

$$H_{QQ} = -\sum_i g_i' \langle O_i \rangle O_i, \tag{5}$$

where g_i' is the quadrupole-quadrupole coupling constant and $\langle O_i \rangle$ is a thermal average of the operator O_i. The Zeeman energy is

$$H_{Zeeman} = -g_j \mu_B J H, \tag{6}$$

where $g_j = 1.25$ is the Landé factor and $J = 8$ is the quantum number of the total angular momentum of a Ho^{3+} ion.

The temperature dependence of an elastic modulus, C_{ii}, can be calculated using the following equation that takes into

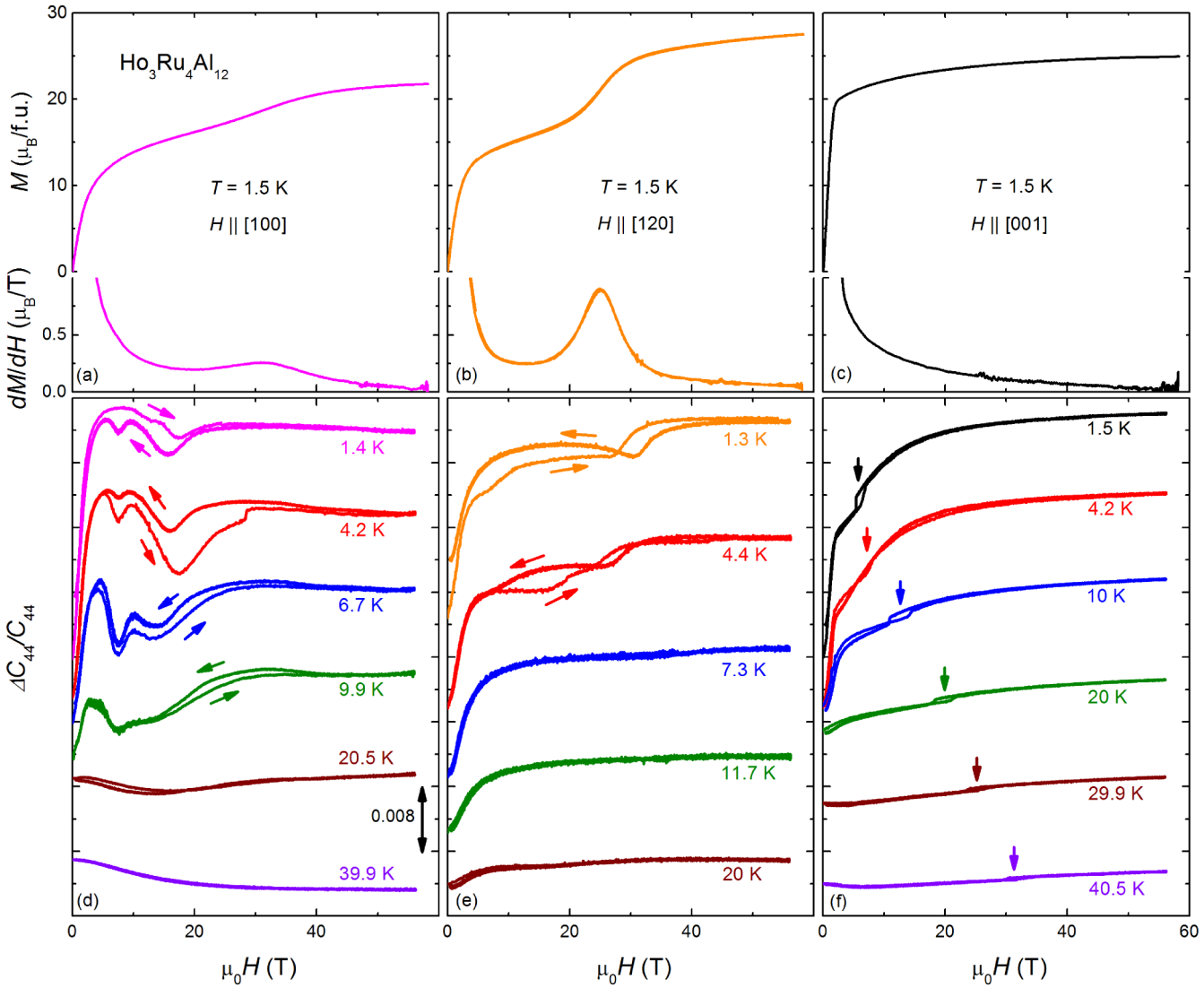

FIG. 5. Magnetization, M, field derivative of the magnetization, dM/dH, and elastic modulus, C_{44}, of $Ho_3Ru_4Al_{12}$ for field applied along the (a, d) [100], (b, e) [120], and (c, f) [001] axes. The ultrasound frequencies were 103, 103, and 136 MHz for field applied along the [100], [120], and [001] axes, respectively.

account quadrupole interaction [39]:

$$C_i(T) = C_i^{(0)}(T) - \frac{N_0 g_i^2 \chi_i^{(s)}(T)}{1 - g_i' \chi_i^{(s)}(T)}, \qquad (7)$$

where $N_0 = 9.462 \times 10^{27}$ m^{-3} is the density of Ho atoms per unit volume, χ_s is a quadrupole susceptibility [35], and $C_i^{(0)}$ is the background stiffness. Since C_{44} displays a softening with decreasing temperature [Fig. 3(c)] and large changes in applied field [Figs. 5(d), 5(e) and 5(f)], we concentrate on this shear elastic modulus. We assume that $C_i^{(0)}$ can be expressed as $a + bT^2 + cT^4$, where the second term is the contribution of the electrons other than the $4f$ electrons and the third term is the phonon contribution [40]. Assuming that at high temperatures, above 150 K, the slopes of C_{44} and $C_{44}^{(0)}$ are nearly the same, a fit to the data $\Delta C_{44}/C_{44}$ above 150 K resulted in $a = 3.5 \times 10^{-2}$, $b = -6.6 \times 10^{-7}$ K^{-2}, and $c = 2.8 \times 10^{-12}$ K^{-4}. Additionally, we calculated the magnetic susceptibility and magnetization for a nonordered state using the CEF model [41]. Details of the calculations are given in the Supplemental Material [30].

Using the crystal-field parameters listed in Table III, our analysis reproduces well the $1/\chi$ vs T dependence in the paramagnetic state [Fig. 6(a)]. The field-dependent magnetization is reproduced qualitatively: The calculated $M(H)$ dependences display an S-shape for the [100] and [120] axes [Fig. 6(b)]. This suggests that these anomalies are caused by CEF effects. Another contribution is likely due to a reorientation of Ho magnetic moments. Note that, akin to the experimental data, there are no features in the magnetization for fields applied along the [001] direction.

TABLE III. CEF parameters, B_m^n (K), for $Ho_3Ru_4Al_{12}$.

B_2^0	B_4^0	B_6^0	B_6^6
–0.35(5)	$1.75(8)\times10^{-3}$	$6.5(8)\times10^{-6}$	$1.2(5)\times10^{-5}$

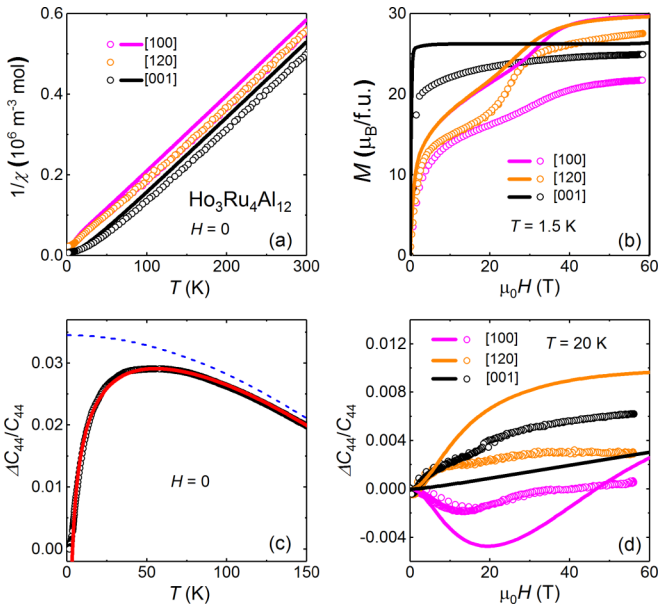

FIG. 6. Temperature dependences of (a) the inverse magnetic susceptibility, $1/\chi$, and (c) the transverse elastic modulus, C_{44}, and field dependences of (b) the magnetization, M, and (d) of C_{44} of $Ho_3Ru_4Al_{12}$. In all panels, the symbols and the solid lines represent the experimental and calculated data, respectively. The dashed line in panel (c) is the background stiffness (see text for details).

For all field directions, the magnetization values found experimentally are lower than the calculated values. There are two main reasons that can explain the reduced magnetic moments. First, the magnetization measurements were taken at a relatively "high" temperature of 1.5 K, which is 1/3 of the Néel temperature, so that the ground-state values of the magnetic moments might be reduced. Second, geometric frustration likely plays an important role. As the Ho atoms form a distorted kagome lattice, their magnetic moments might be subject to competing exchange interactions due to frustration. One may expect an incomplete ordering of the Ho moments at T_N.

The softening of the transverse elastic modulus C_{44} can be well accounted for by Eq. (7), with $|g_i| = 14.36$ K and $g_i' = -2.5 \times 10^{-3}$ K [Fig. 6(c)]. The negative g_i' suggests an antiferroquadrupolar-type interaction.

The importance of a quadrupole interaction also follows from our fits of C_{44} measured in pulsed fields at 20 K [Fig. 6(d)]. For the hexagonal symmetry, the strains ε_{yz} and ε_{zx} that couple to the quadrupoles O_{yz} and O_{zx}, respectively, are degenerate. The degeneracy can be lifted by applied magnetic field. For O_{zx}, we obtain a qualitative agreement between the experimental and calculated data: a minimum is reproduced in C_{44} for fields applied along [100], whereas C_{44} increases for fields applied along [120] and [001]. For O_{yz}, we find opposite $C_{44}(H)$ features for fields applied along [100] and [120]. More information is given in the Supplemental Material [30].

At low temperatures, the magnetic contribution dominates the specific heat. We attempted to suppress the low-temperature magnetic contribution by applying a magnetic field along the [001] axis. The phase transition seen in 0 T is suppressed and no longer observed already at 2 T (Fig. 7). Interestingly, the $C(T)$

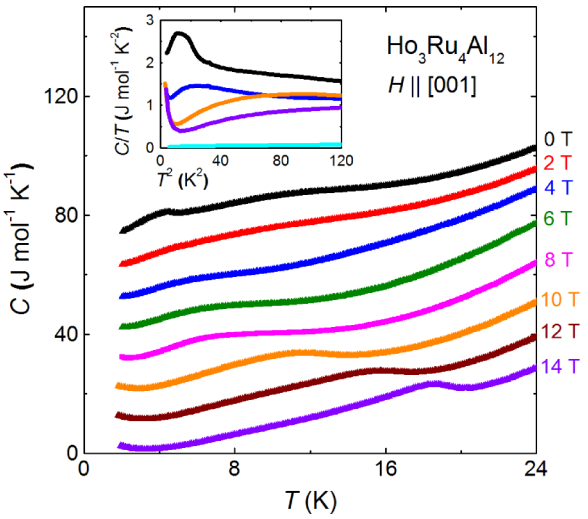

FIG. 7. Temperature dependence of the specific heat of $Ho_3Ru_4Al_{12}$ in various magnetic fields applied along the [001] axis. The curves are vertically offset for clarity. The inset shows C/T vs T^2 data at 0, 4, 10, and 14 T. In the inset, the cyan curve is the $C/T(T^2)$ dependence of $Y_3Ru_4Al_{12}$.

data for higher fields show an additional anomaly that develops and shifts to higher temperatures with increasing field. The C/T vs T^2 data for nonmagnetic $Y_3Ru_4Al_{12}$ as compared to those of $Ho_3Ru_4Al_{12}$ give a rough estimate of the negligible (itinerant) electron and phonon contribution to the total specific heat (inset in Fig. 7). At low temperatures in the highest applied fields, the specific heat displays an upturn. This reflects an additional nuclear contribution, as holmium has a very strong hyperfine interaction [42,43].

Based on the crystal-field parameters listed in Table III and our experimental observations, we propose the following CEF scheme (Fig. 8). In a hexagonal CEF, the 17-fold multiplet of a Ho^{3+} ion splits into five singlets and six doublets. The

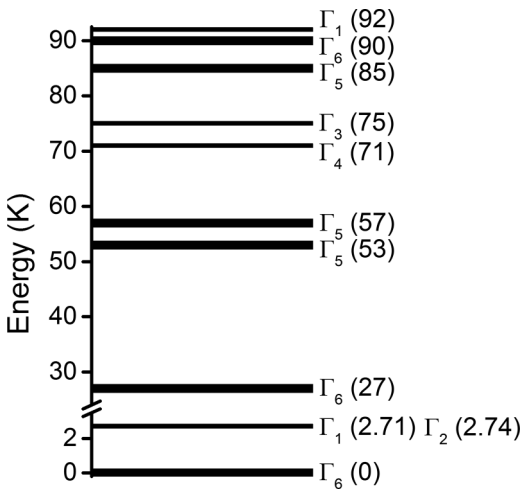

FIG. 8. CEF level scheme of a Ho^{3+} ion in $Ho_3Ru_4Al_{12}$ obtained from the CEF parameters listed in Table III. The thin lines represent singlets, the thick lines represent doublets. For the low-energy singlets Γ_1 and Γ_2, the error bars are 0.5 K. For higher CEF levels, the error bars are somewhat larger.

TABLE IV. Wave functions, $|J, J_z\rangle$ ($J = 8$), of the quasiquartet for $Ho_3Ru_4Al_{12}$.

Ground state (Γ_6)	$0.99996\|-7\rangle - 0.00896\|-1\rangle + 0.00054\|5\rangle$ $-0.00054\|-5\rangle + 0.00896\|1\rangle - 0.99996\|7\rangle$
First excited state (Γ_1)	$-0.69678\|-6\rangle + 0.01986\|0\rangle - 0.71701\|6\rangle$
Second excited state (Γ_2)	$-0.71715\|-6\rangle + 0.00028\|0\rangle + 0.69692\|6\rangle$

ground-state doublet with the symmetry Γ_6 is separated by 2.71 K from the first excited singlet Γ_1 and by 2.74 K from the second excited singlet Γ_2. The next doublet, Γ_6, lies at 27 K, which can explain the broad Schottky-like anomaly observed in the specific heat at around 12 K [inset in Fig. 2(b)]. The maximum splitting of the CEF scheme is just below 100 K.

Due to the crystal symmetry, for the ground-state doublet Γ_6, the matrix elements $\langle\Gamma_6|O_{yz}|\Gamma_6\rangle$ and $\langle\Gamma_6|O_{zx}|\Gamma_6\rangle$ are zero. This means Γ_6 has no quadrupolar degeneracy corresponding to the C_{44} mode. However, the ground-state doublet and the first two excited singlets at about 2.7 K form a quasiquartet. Both matrix elements for O_{yz}, $\langle\Gamma_6|O_{yz}|\Gamma_1\rangle$ and $\langle\Gamma_6|O_{yz}|\Gamma_2\rangle$, and for O_{zx}, $\langle\Gamma_6|O_{zx}|\Gamma_1\rangle$ and $\langle\Gamma_6|O_{zx}|\Gamma_2\rangle$, have a nonzero value. This suggests the existence of an interlevel quadrupolar interaction between the ground-state doublet and the excited levels of the quasidegenerate states. The wave functions for the quasiquartet are given in Table IV. (A complete set of wave functions can be found in the Supplemental Material [30].) Thus, the CEF scheme supports our interpretation of the temperature and field dependence of C_{44} that can be explained by quadrupolar interaction.

In applied field, the Zeeman energy competes with exchange interactions and the magnetocrystalline anisotropy. The energy scale of the leading magnetic exchange is given by the Weiss temperature. For $H||[001], \theta = 27$ K. The magnetic anisotropy energy can be estimated using Eq. (3) and the CEF parameters (Table III). The CEF parameters show that only the first term in Eq. (3) is important, the other terms can be neglected. Using ${O_2}^0 = 118.7$ for Ho^{3+} (see, e.g., [27]), we obtain ${B_2}^0{O_2}^0 \approx$ -42 K. Thus, the magnetic anisotropy energy is comparable to the leading magnetic exchange.

Further, we calculated the field dependences of the CEF states (Fig. 9). These data suggest that level crossings occur within the ground-state doublet. Applied fields lift the degeneracy of the ground-state doublet. The Zeeman splitting leads to a level crossing at approximately 30 and 20 T for fields applied along the [100] and [120] axes, respectively [Figs. 9(a) and 9(b)]. These fields correspond to the regions where field-induced anomalies in $M(H)$ are observed [Figs. 5(a) and 5(b)]. For fields applied along the [001] axis, no level crossing appears up to 60 T [Fig. 9(c)], in accordance with our experimental observations.

V. CONCLUSION

Our results show that the magnetic and magnetoelastic properties of the antiferromagnet $Ho_3Ru_4Al_{12}$ result from an interplay between CEF effects and geometric frustrations. The Ho magnetic moments order at $T_N = 4.5$ K. In the applied field, the magnetization displays anomalies due to CEF transitions. The absolute values of the Ho magnetic moments are reduced, which suggests their frustrated character.

The proposed CEF scheme of the Ho^{3+} ion shows a quasiquartet below about 2.7 K. Interlevel transitions allow for a quadrupolar interaction. Taking them into account reproduces well the temperature and field dependences of the shear elastic modulus C_{44}. Obviously, the ground-state quartet significantly renormalizes C_{44}. Due to symmetry reasons, other elastic moduli are not strongly affected.

ACKNOWLEDGMENTS

We acknowledge the support of HLD at HZDR, member of the European Magnetic Field Laboratory (EMFL). The work was supported by the Materials Growth and Measurement Laboratory (MGML, https://mgml.eu), by Grant No. 16-03593S of the Czech Science Foundation, and by the DFG through SFB 1143. M.S.H. also acknowledges the Project No. LO1603 under the Ministry of Education, Youth and Sports National sustainability programme I of Czech Republic.

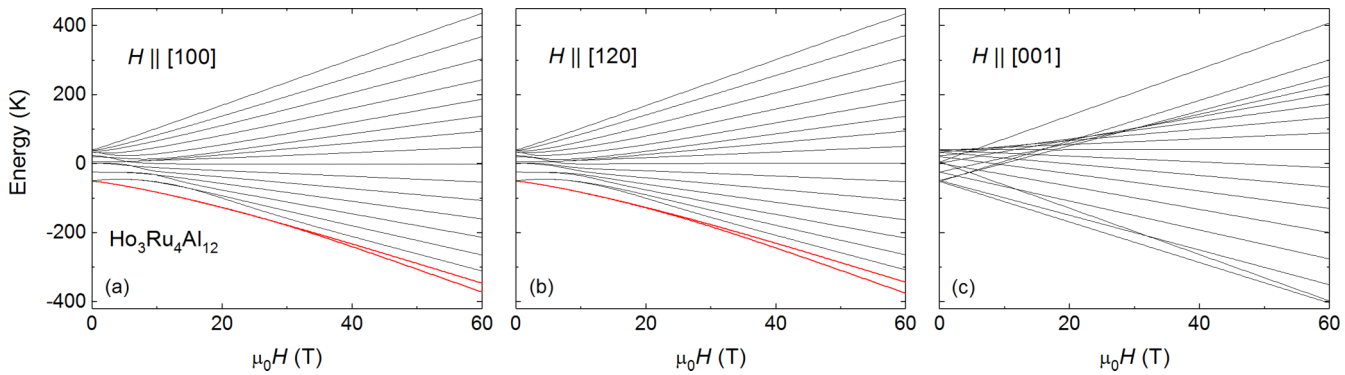

FIG. 9. Field dependences of the CEF states for field applied along the (a) [100], (b) [120], and (c) [001] axes of $Ho_3Ru_4Al_{12}$. In panels (a) and (b), the red curves are those of the ground-state doublet.

[1] A. P. Ramirez, in *Handbook of Magnetic Materials*, edited by K. H. J. Buschow (Elsevier, Amsterdam, 2001), Vol. 13.

[2] J. S. Gardner, M. J. P. Gingras, and J. E. Greedan, Rev. Mod. Phys. **82**, 53 (2010).

[3] M. J. P. Gingras, C. V. Stager, N. P. Raju, B. D. Gaulin, and J. E. Greedan, Phys. Rev. Lett. **78**, 947 (1997).

[4] S. P. Bramwell and M. J. P. Gingras, Science **294**, 1495 (2001).

[5] J. E. Greedan, J. Alloys Compd. **408-412**, 444 (2006).

[6] H. D. Zhou, C. R. Wiebe, A. Harter, N. S. Dalal, and J. S. Gardner, J. Phys.: Condens. Matter **20**, 325201 (2008).

[7] B. Normand and Z. Nussinov, Phys. Rev. Lett. **112**, 207202 (2014).

[8] R. Sibille, E. Lhotel, M. C. Hatnean, G. Balakrishnan, B. Fåk, N. Gauthier, T. Fennell, and M. Kenzelmann, Phys. Rev. B **94**, 024436 (2016).

[9] J. J. Wen, S. M. Koohpayeh, K. A. Ross, B. A. Trump, T. M. McQueen, K. Kimura, S. Nakatsuji, Y. Qiu, D. M. Pajerowski, J. R. D. Copley, and C. L. Broholm, Phys. Rev. Lett. **118**, 107206 (2017).

[10] R. E. Gladyshevskii, O. R. Strusievicz, K. Cenzual, and E. Parthé, Acta Cryst. B **49**, 474 (1993).

[11] J. Niermann and W. Jeitschko, Z. Anorg. Allg. Chem. **628**, 2549 (2002).

[12] N. G. Bukhan'ko, A. I. Tursina, S. V. Malyshev, A. V. Gribanov, Y. D. Seropegin, and O. I. Bodak, J. Alloys Compd. **367**, 149 (2004).

[13] W. Ge, H. Ohta, C. Michioka, and K. Yoshimura, J. Phys.: Conf. Series **344**, 012023 (2012).

[14] W. Ge, C. Michioka, H. Ohta, and K. Yoshimura, Solid State Commun. **195**, 1 (2014).

[15] D. I. Gorbunov, M. S. Henriques, A. V. Andreev, V. Eigner, A. Gukasov, X. Fabrèges, Y. Skourski, V. Petříček, and J. Wosnitza, Phys. Rev. B **93**, 024407 (2016).

[16] M. S. Henriques, D. I. Gorbunov, A. V. Andreev, X. Fabrèges, A. Gukasov, M. Uhlarz, V. Petříček, B. Ouladdiaf, and J. Wosnitza, Phys. Rev. B **97**, 014431 (2018).

[17] V. Chandragiri, K. K. Iyer, and E. V. Sampathkumaran, J. Phys.: Condens. Matter **28**, 286002 (2016).

[18] D. I. Gorbunov, S. Henriques, A. V. Andreev, Y. Skourski, and M. Dušek, J. Alloys Compd. **634**, 115 (2015).

[19] S. K. Upadhyay, K. K. Iyer, and E. V. Sampathkumaran, J. Phys.: Condens. Matter **29**, 325601 (2017).

[20] D. I. Gorbunov, M. S. Henriques, A. V. Andreev, A. Gukasov, V. Petříček, N. V. Baranov, Y. Skourski, V. Eigner, M. Paukov, J. Prokleška, and A. P. Gonçalves, Phys. Rev. B **90**, 094405 (2014).

[21] V. Chandragiri, K. K. Iyer, and E. V. Sampathkumaran, Intermetallics **76**, 26 (2016).

[22] I. Ishii, K. Takezawa, H. Goto, S. Kamikawa, A. V. Andreev, D. I. Gorbunov, M. S. Henriques, and T. Suzuki, J. Phys.: Conf. Series **807**, 012002 (2017).

[23] S. Nakamura, S. Toyoshima, N. Kabeya, K. Katoh, T. Nojima, and A. Ochiai, JPS Conf. Proc. **3**, 014004 (2014).

[24] S. Nakamura, S. Toyoshima, N. Kabeya, K. Katoh, T. Nojima, and A. Ochiai, Phys. Rev. B **91**, 214426 (2015).

[25] M. Pasturel, O. Tougait, M. Potel, T. Roisnel, K. Wochowski, H. Noël, and R. Troć, J. Phys.: Condens. Matter **21**, 125401 (2009).

[26] R. Troć, M. Pasturel, O. Tougait, A. P. Sazonov, A. Gukasov, C. Sułkowski, and H. Noël, Phys. Rev. B **85**, 064412 (2012).

[27] J. J. M. Franse and R. J. Radwański, in *Handbook of Magnetic Materials*, edited by K. H. J. Buschow (Elsevier, Amsterdam, 1993), Vol. 7.

[28] M. D. Kuz'min and J. M. D. Coey, Phys. Rev. B **50**, 12533 (1994).

[29] A. Sippel, L. Jahn, M. Loewenhaupt, D. Eckert, P. Kerschl, A. Handstein, K.-H. Müller, M. Wolf, M. D. Kuz'min, L. Steinbeck, M. Richter, A. Teresiak, and R. Bewley, Phys. Rev. B **65**, 064408 (2002).

[30] See Supplemental Material at http://link.aps.org/supplemental/10.1103/PhysRevB.97.184412 for additional experimental data (Laue diffraction patterns and elastic moduli at elevated temperatures) and crystal-electric-field analysis.

[31] CRYSALIS PRO, Agilent Technologies, Version 1.171.37.31.

[32] L. Palatinus and G. Chapuis, J. Appl. Cryst. **40**, 786 (2007).

[33] V. Petříček, M. Dušek, and L. Palatinus, Z. Kristallogr. **229**, 345 (2014).

[34] B. Wolf, B. Lüthi, S. Schmidt, H. Schwenk, M. Sieling, S. Zherlitsyn, and I. Kouroudis, Phys. B **294–295**, 612 (2001).

[35] B. Lüthi, *Physical Acoustics in the Solid State* (Springer, Heidelberg, 2005).

[36] Y. Skourski, M. D. Kuz'min, K. P. Skokov, A. V. Andreev, and J. Wosnitza, Phys. Rev. B **83**, 214420 (2011).

[37] M. S. Henriques *et al.* (unpublished).

[38] M. T. Hutchings, Solid State Phys. **16**, 227 (1964).

[39] B. Lüthi, in *Dynamical Properties of Solids*, edited by G. K. Horton and A. A. Maradudin (North-Holland, Amsterdam, 1980), Vol. 3.

[40] M. Nohara, T. Suzuki, Y. Maeno, T. Fujita, I. Tanaka, and H. Kojima, Phys. Rev. B **52**, 570 (1995).

[41] N. V. Hieu, T. Takeuchi, H. Shishido, C. Tonohiro, T. Yamada, H. Nakashima, K. Sugiyama, R. Settai, T. D. Matsuda, Y. Haga, M. Hagiwara, K. Kindo, S. Araki, Y. Nozue, and Y. Onuki, J. Phys. Soc. Jap. **76**, 064702 (2007).

[42] J. E. Gordon, C. W. Dempesy, and T. Soller, Phys. Rev. **124**, 724 (1961).

[43] O. V. Lounasmaa, Phys. Rev. **128**, 1136 (1962).